Angular Dependence of Nonlinear Thomson Scattering From Electrons in a High Intensity Laser Focus

Christoph Schulzke

A thesis submitted to the faculty of
Brigham Young University
in partial fulfillment of the requirements for the degree of

Master of Science

Michael Ware, Chair
Justin Peatross
Richard Sandberg

Department of Physics and Astronomy

Brigham Young University

ABSTRACT

Angular Dependence of Nonlinear Thomson Scattering
From Electrons in a High Intensity Laser Focus

Christoph Schulzke
Department of Physics and Astronomy, BYU
Master of Science

The theory of nonlinear Thomson scattering is presented. A model for the scattered light is developed. The orthogonal polarizations of the second harmonic of the scattered light are examined. The predictions of the model are compared to measurements by our group in collaboration with the Extreme Light Laboratory at the University of Nebraska-Lincoln (UNL). The veracity of the theory and model are confirmed by comparison to the experimental data.

Keywords: high-intensity lasers, nonlinear Thomson scattering

ACKNOWLEDGMENTS

This research was supported by a grant funded by the National Science Foundation. My research would not have been possible without the mentorship of Dr. Ware and Dr. Peatross. The measurements presented in this research were done at the Extreme Light Laboratory at UNL operated by the research group of Dr. Don Umstadter. The help of Colton Fruhling, in particular, was instrumental in taking the measurements presented here.

Contents

Chapter 1

Nonlinear Thomson Scattering

1.1 Electrons in a Laser Field

The interaction between electrons and electromagnetic fields have been of interest since the discovery of the electron [1]. The fields and particles are coupled by Maxwell's equation [2] and the Lorentz force law [3]. Thomson scattering, the elastic scattering of radiation, was first described by J. J. Thomson in 1906 [4]. After the development of laser technologies, nonlinear Thomson scattering became an active field of research [5–7]. It was not until after the development of chirped pulse lasers [8] that these effects could be observed [10–20]. Our group at BYU has researched this phenomenon extensively and continues work in this area [19–21].

The motion of an electron with momentum *vecp* within an electromagnetic field, represented by the vectors **E** and **B**, is dictated by the Lorentz force [3]

$$\frac{d\mathbf{p}}{dt} = e\left(\mathbf{E} + \mathbf{u} \times \mathbf{B}\right) \tag{1.1}$$

where e is the elementary charge. If **E** and **B** are known, then we can solve this equation for the trajectory of the electron, ignoring radiation reaction. As long as $|\mathbf{u}| << c$, the contribution from the magnetic field can be neglected and the Lorentz force law is a linear differential equation. In the

case that $|\mathbf{u}|$ is a significant fraction of the speed of light, the contribution from the magnetic field can no longer be ignored and the Lorentz force law develops nonlinear characteristics. Generally, there is not an analytic solution to this problem and the equation is solved numerically.

Within this relativistic regime the electron's momentum vector $\mathbf{p}$ is defined as

$$\mathbf{p} = m\mathbf{u}\gamma \tag{1.2}$$

where the Lorentz factor, γ, is defined by

$$\gamma = \frac{1}{\sqrt{1-u^2/c^2}} \tag{1.3}$$

Where again, so long as $|\mathbf{u}| << c$, the Lorentz factor remains $\simeq 1$ and relativistic effects are negligible. Intensities greater than 10^{17} W/cm^2 are needed to reach the relativistic regime with near infrared light. These intensities can be reached by tightly focusing a high power laser pulse. Interactions of this kind were worked out in theory [5–7] about 20 years before Bucksbaum et al. were able to observe the relativistic scattering of electrons from a laser focus [14]. The development of ultra-short pulsed lasers [8] made the observation of these effects more practical [10–13].

If we model a laser pulse as an elliptically polarized plane wave, we can arrive at an analytic description of this interaction. While a plane wave is not a true physical situation, we can build intuition for a real laser focus by studying this simplified problem. A laser of arbitrary elliptical polarization traveling in the $\hat{z}$ direction can be expressed in the form

$$\mathbf{E} = E_0(\phi_L)\left[\hat{\mathbf{x}}\sqrt{1-\delta^2}\cos\phi_L + \hat{\mathbf{y}}\delta\sin\phi_L\right] \tag{1.4}$$

$$\mathbf{B} = \frac{E_0(\phi_L)}{c}\left[-\hat{\mathbf{x}}\delta\sin\phi_L + \hat{\mathbf{y}}\sqrt{1-\delta^2}\cos\phi_L\right] \tag{1.5}$$

where ϕ_L is the phase of the laser and is given by

$$\phi_L = \frac{\omega}{c}z - \omega t \tag{1.6}$$

and δ is a parameter that controls the ellipticity of the laser polarization that ranges from 0 to 1. If $\delta = 0$, then the laser is polarized in the $\hat{x}$ direction; if $\delta = 1$, then the laser is polarized in the $\hat{y}$;

and if $\delta = \frac{1}{\sqrt{2}}$ the laser is circularly polarized. Intermediate values of δ yield intermediate laser polarizations. While not the topic of this thesis, I also assisted in measuring the effects of varying the polarization. That research is being conducted by Colton Fruhling at UNL.

If the envelope function $E_0(\phi)$ is assumed to vary slowly with ϕ and to start from zero, then the solution to the Lorentz force law with Eqs. (1.4) and (1.5) used for the fields is

$$\frac{\mathbf{u}}{c} \simeq \frac{1}{\gamma}\left[\gamma_0 \frac{\mathbf{u}_0}{c} - \hat{\mathbf{x}}\alpha\sqrt{1-\delta^2}\sin\phi_L + \hat{\mathbf{y}}\alpha\delta\cos\phi_L + \hat{\mathbf{z}}(\gamma-\gamma_0)\right] \tag{1.7}$$

Variables with subscript 0 are the value of the variable before the pulse has arrived. The parameter α is the scaled magnitude of the electric field and can be defined in terms of the intensity I [16, 22]

$$\alpha = \frac{eE}{kmc^2} = \frac{e\lambda}{\pi mc^2}\sqrt{\frac{I}{2\varepsilon_0 c}} = 0.85\left(\frac{\lambda}{1\ \mu\text{m}}\right)\sqrt{\frac{I}{10^{18}\ \text{W/cm}^2}} \tag{1.8}$$

where λ is the wavelength of the laser, and ε_0 is the permittivity of free space. From Eq. (1.7) we can immediately see that increasing the intensity of the laser field directly increases the magnitude of the velocity in the $\hat{\mathbf{x}}$ and $\hat{\mathbf{y}}$ directions. Increasing the intensity also increases a drift velocity in the $\hat{z}$ direction, but that increase is tied into the γ factor.

Taking the derivative of Eq. (1.7) with respect to time gives us the acceleration $\mathbf{a}$. For simplicity, we change the time derivative to a derivative with respect to the phase by using $\frac{d\phi_L}{dt} = \frac{\omega}{c}u_z - \omega$. Using these we get

$$\mathbf{a} = \frac{d\mathbf{u}}{dt} = \frac{d\mathbf{u}}{d\phi_L}\frac{d\phi_L}{dt} = -\omega\left(1-\frac{u_z}{c}\right)\frac{d\mathbf{u}}{d\phi_L} \tag{1.9}$$

Conversely, if we integrate Eq. (1.7) to get the position $\mathbf{r}$

$$\frac{d\mathbf{r}}{dt} = \frac{d\mathbf{r}}{d\phi_L}\frac{d\phi}{dt} \quad \Rightarrow \quad \mathbf{r} = -\frac{1}{\omega\gamma_0\left(1-\frac{u_{z0}}{c}\right)}\int_0^{\phi_L}\gamma\mathbf{u}\,d\phi_L' \tag{1.10}$$

where we integrate the phase from the beginning of the interaction where $\phi_L = 0$ up to the point we are interested in at ϕ_L.

The average velocity of the particle as it drifts in the direction of laser propagation is

$$\mathbf{u}_{ave} = \frac{\mathbf{u}_0 + \hat{\mathbf{z}}c\tilde{\alpha}^2/4}{1+\tilde{\alpha}^2/4} \qquad \text{where} \qquad \tilde{\alpha} = \frac{\alpha}{\gamma_0\sqrt{1-u_{z0}/c}} \tag{1.11}$$

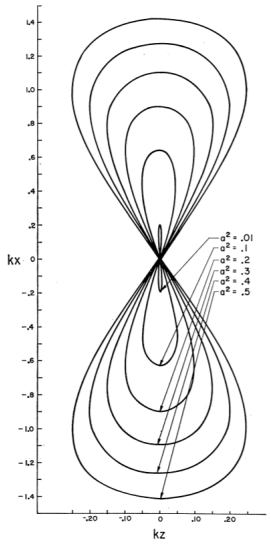

Figure 1.1 The trajectory of an electron within its average rest frame. The electron is experiencing a plane wave laser field propagating in the y-direction and laser polarized in the x-direction. The axises are scaled to the wavelength. The different sizes of figure-eights correspond to different values of α. As α increases, corresponding to a stronger laser intensity, the length of the track approaches one wavelength, which implies the electron is approaching the speed of light. This figure was first presented by Sarachik and Schappert along with their solution to an electron's trajectory within its average rest frame [6].

The solution to the particles motion within its average rest frame was worked out by Sarachik and Schappert in 1970 [6]. They found that the trajectory in the average rest frame of the electron is the figure-eight shape shown in Fig. 1.1. The effect of increasing the intensity of the field is seen as the concentric figure-eight shapes get larger. As increasingly powerful forces are exerted on an electron, the figure-eight trajectory gets larger and the electron experiences larger accelerations. The electron will radiate light according to Maxwell's equations [2]. Due to the nonlinear forces at play, harmonics of the laser frequency are scattered in addition to the fundamental frequency.

1.2 Laser Driven Electron Radiation

The radiation of nonlinear Thomson scattering has been studied thoroughly [6, 16]. Previous work on the topic treats electrons as particles because quantum effects are negligible. The use of this semi-classical approach is justified by theory [5] and experiment [21]. The assumption of electrons as point emitters is used here as well.

For an electron experiencing an acceleration **a** with a velocity **u**, the observed radiation is given by the far-field radiation formula [23]

$$\mathbf{E} = \frac{e}{4\pi\varepsilon_0 c R_d} \frac{\hat{\mathbf{R}}_d \times \left(\left(\hat{\mathbf{R}}_d - \frac{\mathbf{u}}{c}\right) \times \frac{\mathbf{a}}{c}\right)}{\left(1 - \hat{\mathbf{R}}_d \cdot \frac{\mathbf{u}}{c}\right)^3} \tag{1.12}$$

where $\hat{\mathbf{R}}_d$ is the unit vector pointing from the electron to the detector at time t. However, the velocity, **u**, and acceleration, **a**, are both evaluated at the retarded time t_r given by

$$t_r = t - \left(R_d - \mathbf{r} \cdot \mathbf{R}_d\right)/c \tag{1.13}$$

We know that as $|\mathbf{u}|$ becomes large, harmonics of the laser light will be scattered. To investigate the frequency makeup of the scattered radiation, we take the Fourier transform of Eq. (1.12)

$$\mathbf{E}(\omega) = \frac{e}{4\pi\varepsilon_0 c R_d} \frac{1}{\sqrt{2\pi}} \int_{-\infty}^{\infty} \frac{\hat{\mathbf{R}}_d \times \left(\left(\hat{\mathbf{R}}_d - \frac{\mathbf{u}}{c}\right) \times \frac{\mathbf{a}}{c}\right)}{\left(1 - \hat{\mathbf{R}}_d \cdot \frac{\mathbf{u}}{c}\right)^3} e^{i\omega t} dt \tag{1.14}$$

By rearranging Eq. (1.14) and using Eq. (1.13) to change the variable of integration to the retard time t_r we arrive at

$$\mathbf{E}(\omega) = i\omega \frac{e}{4\pi\varepsilon_0 c R_d} \frac{1}{\sqrt{2\pi}} \int_{-\infty}^{\infty} \hat{\mathbf{R}}_d \times \left(\hat{\mathbf{R}}_d \times \frac{\mathbf{u}}{c}\right) e^{i\omega\left(t_r + \frac{1}{c}(R_d - \mathbf{r}\cdot\hat{\mathbf{R}}_d)\right)} dt_r \tag{1.15}$$

This form is not particularly useful for seeing the exact harmonics of the scattered light. It is convenient to change the variable of integration to the laser phase ϕ_L using the relation $t_r - \frac{z}{c} = -\frac{\phi_L}{\omega_0} \Rightarrow dt_r = -\frac{d\phi_L}{\omega_0\left(1 - \frac{u_z}{c}\right)}$ where ω_0 is the angular frequency of the laser. This will also be the

fundamental frequency of the scattered light. In addition to changing the variable of integration to ϕ_L, we also write the frequency in terms of the harmonic order using $\omega = N\omega_0$ where N is a whole number representing the harmonic order of the scattered light.

$$\mathbf{E}(N) = -ie^{-iNR_d\omega_0/c}\frac{q}{4\pi\varepsilon_0 cR_d}\frac{1}{\gamma_0\left(1-\frac{u_{z0}}{c}\right)}\frac{Nn}{\sqrt{2\pi}}\int_0^{2\pi}\hat{\mathbf{R}}_d\times\left(\hat{\mathbf{R}}_d\times\gamma\frac{\mathbf{u}}{c}\right)e^{iN\left(\phi_L+\omega_0(\mathbf{r}\cdot\hat{\mathbf{R}}_d-z)/c\right)}d\phi \tag{1.16}$$

it is important to note that we are only integrating over one cycle of the laser and we have introduced the variable n which represents the number of cycles in the laser pulse. Note that $\mathbf{E}(\omega)$ was changed into $\mathbf{E}(N)$ since the equation has been rewritten in terms of the harmonic order. As we can see, the integral is not generally zero for $N \neq 1$. The analytic solution to the radiation scattered by an electron within a plane wave is found by substituting Eq. (1.7) and Eq. (1.10) into Eq. (1.16).

The spectrum for Thomson scattering from a plane wave pulse is shown in Fig. 1.2 for a detector positioned at $\theta = \pi/4$ and $\phi = 0$, using traditional spherical coordinates where the z axis is defined by the laser beam. In Fig. 1.2a we see the spectrum from a pulse with intensities corresponding to $\alpha = 0.25$. At this low intensity, nonlinear Thomson scattering is barely observable. In Fig. 1.2b we see the spectrum from a pulse with $\alpha = 0.8$. Note the clear harmonic orders of the scattered light. This allows for the use of band-pass filters in narrowing the frequency band of the detected radiation and thereby reducing noise.

If we focus on the second harmonic scattered from a plane wave with $\alpha = 0.8$, we observe the radiation pattern shown in Fig. 1.3. The scattered radiation has been resolved into a component parallel to the wave's direction of propagation and a component perpendicular to the direction of propagation.. The perpendicular polarization exhibits symmetry with respect to the polar angle as well as fourfold azimuthal symmetry. The parallel component lacks the polar symmetry and has only a twofold symmetry with respect to the azimuthal angle. The preference towards the 'downstream' side of the pulse is due to the drift velocity, given in Eq. (1.11), as well as the asymmetry in the trajectory shown in Fig. 1.1, namely that the electron is moving in the same direction at both the top

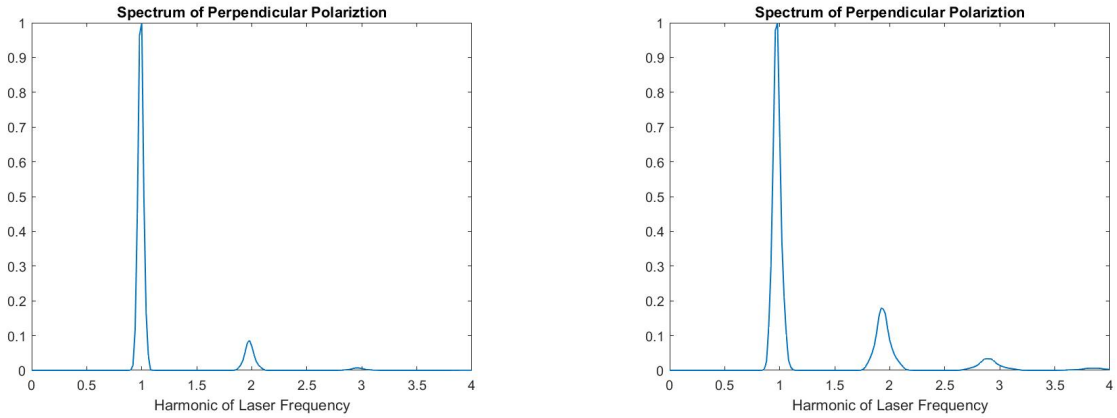

(a) **(b)**

Figure 1.2 The frequency makeup of radiation scattered by 5000 electrons. The detector is positioned at $\theta = \pi/4$ and $\phi = 0$. The electrons are initially at rest and randomly positioned. Each electron's spectrum is plotted in its own color. In (a) we see linear Thomson scattering from a pulse with intensities corresponding to $\alpha = 0.25$. In (b) we can see the harmonic generation that occurs when $\alpha = 0.8$.

and bottom of the figure-eight. The exact dependence can be seen by taking the inner product of the spherical unit vectors $\hat{\theta} = \cos\theta\cos\phi\hat{\mathbf{x}} + \cos\theta\sin\phi\hat{\mathbf{y}} - \sin\theta\hat{\mathbf{z}}$ and $\hat{\phi} = -\sin\phi\hat{\mathbf{x}} + \cos\phi\hat{\mathbf{y}}$ with Eq. (1.16).

1.3 Lorentz Boost

It is important to note that due to the drift of the particle, the scattered radiation is Doppler shifted [16]. This shift is proportional to the intensity of the laser. The shifted frequency ω_0' is given by

$$\omega_0' = \omega_0 \frac{1}{\gamma(1 + u_z\cos\theta)} \tag{1.17}$$

in terms of the wavelength this is

$$\lambda' = \lambda\gamma(1 + u_z\cos\theta) \tag{1.18}$$

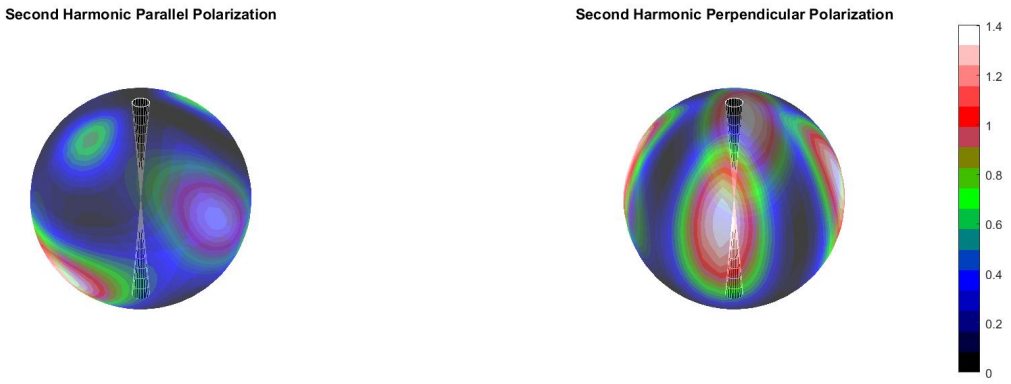

(a) **(b)**

Figure 1.3 Second harmonic Thomson scattering from a plane wave with $\alpha = 0.8$. The wave propagates from top to bottom. The electrons are placed at the center of the sphere. Areas with higher intensities of scattering are shown in red while low intensity areas are shown in blue. The polarization parallel to the wave's propagation direction is shown in (a). The perpendicular polarization is shown in (b). The interaction of 500 randomly placed electrons was simulated to generate these radiation patterns.

Where we use the average velocity in Eq. (1.7) for u_z and in the relativistic factor. The transformation applies to all scattered wavelengths, so the spectrum shown in Fig. 1.2 is not distorted aside from the shift. For a detector position at $\theta = \pi/4$ and a laser with $\alpha = 0.8$, we will observe a fundamental frequency of 887 nm instead of 800 nm. My thesis is focused on the measurement of the second harmonic for which we should expect 443 nm rather than the 400 nm harmonic of the laser.

The redshift allows us to distinguish between the scattered light and the laser light through the use of bandpass filters. Ideally, filters should be centered on the shifted frequencies. At the intensity corresponding to $\alpha = 0.8$ the signal for the second harmonic is fairly broad, ranging from $1.7\omega_L$ and to around 2.1ω. This is much broader than our 10 nm wide bandpass filters, which we center on the red-shifted distribution.

1.4 Overview

The subject of my research is the radiation scattered in the direction of $\theta = \pi/4$ relative to the propagation of laser beam. Past research in this area has focused on the radiation scattered perpendicularly to the beam, within the plane of the laser focus [16, 17, 19–21]. The radiation scattered at $\theta = \pi/4$ displays distinct features from the perpendicular radiation and can be utilized as a second reference in diagnosing a laser focus.

To study the radiation scattered at $\theta = \pi/4$ I first develop a model for simulating the interaction of 1000 electrons randomly dispersed throughout the focal volume. The figures presented in this thesis were produced using my model.

My analysis is applied to linearly polarized laser with $\delta = 0$ in Eq. (1.4). While the model can be generalized to consider any harmonic of the scattered light, we constrained our observations to the second harmonic. The model assumes an ideal azimuthally symmetric Gaussian and I do not consider beam aberrations or nonuniformities.

The model is compared to observations done at the Extreme Light Laboratory at UNL in collaboration with the research group of Dr. Don Umstadter. I participated in the collaboration and helped in the experimental setup and analysis of the data. My analysis shows that the model is in reasonable agreement with these observations.

Chapter 2

Model of Scattering From a Laser Focus

2.1 Scattering From a Laser Focus

In order to achieve the necessary intensities to observe nonlinear Thomson scattering, a high power laser pulse must be focused to a small point. The localization results in strong electromagnetic field gradients. These gradients, which give rise to a ponderomotive force, push the electron out of the laser focus [11–15, 24]. As electrons flee to lower intensity regions, they stop scattering the laser light. This has a significant impact of the overall radiation pattern observed around the laser focus. The case of a plane wave therefore does not fit experimental data taken with real laser focuses. In order to create an effective model of nonlinear Thomson scattering, we must use a more accurate model of a laser focus.

The exact solution to Maxwell's equations for a laser focus was worked out by V. S. Ignatovsky in 1920 [25–27]. This solution involves a computationally expensive integral formula. There are several models of laser focuses which are less computationally expensive. Previous work by Dr. Peatross and Dr. Ware at BYU was done to compare these models to the exact Ignatovsky result [28]. They concluded that the analytical Singh model [29] agrees well with the Ignatovsky solutions. The

Singh model is also computationally efficient. We use the model in our analysis. The Singh model for the focus of a laser polarized in the x-direction and propagating in the z-direction is represented by

$$\mathbf{E}_{\text{Singh}} = E_0 \left[\hat{\mathbf{x}} + \frac{xy}{2\mathbb{Z}^2}\hat{\mathbf{y}} - i\frac{x}{\mathbb{Z}}\hat{\mathbf{z}}\right] \varepsilon \psi^{(0)} e^{i(kz-\omega t)} \tag{2.1}$$

$$\mathbf{B}_{\text{Singh}} = \frac{E_0}{c}\left[\frac{xy}{2\mathbb{Z}^2}\hat{\mathbf{x}} + \hat{\mathbf{y}} - i\frac{y}{\mathbb{Z}}\hat{\mathbf{z}}\right] \varepsilon \psi^{(0)} e^{i(kz-\omega t)} \tag{2.2}$$

where E_0 is the magnitude of the electric field and $\mathbb{Z} = z_0 + iz$. There are several other quantities that must be defined in this model. First there is an envelope function localizing the pulse in time and space

$$\varepsilon = e^{-\frac{\left(t-\frac{z+\rho^2/(2R)}{c}\right)^2}{\tau^2}} \tag{2.3}$$

were $R = z + \frac{z_0^2}{z}$, $\rho = \sqrt{x^2+y^2}$, and τ is the pulse duration. We also have the lowest order Gaussian beam given by

$$\psi^{(0)} = \frac{z_0}{\mathbb{Z}} e^{-\frac{\rho^2}{2\mathbb{Z}}} \tag{2.4}$$

Note that the quantities z_0 and w_0 are the Rayleigh range and beam waist, respectively, related to each other by $z_0 = \frac{kw_0^2}{2}$.

These fields are significantly more complicated then the fields in Eq. (1.4) and Eq. (1.5). This makes finding an analytic solution to the Lorentz force problem intractable. Computational methods are needed in order to model this. Since an analytic solution to the trajectory cannot be generated, an analytic description of the radiation defined in Eq. (1.12) is not possible either. However, after solving the trajectory computationally, the velocity and acceleration arrays can be used to solve for the scattered radiation using the methods outlined in Sec. 1.2.

2.2 Modeling of Thomson Scattering

The code for this model is found in Appendix A. We utilized the Matlab programming environment. All variables are scaled for simplifying the code. Distances are scaled according $r' = kr$ where k is the wavenumber of the laser. Times are scaled according to $t' = \omega t$ where ω is the angular frequency of the laser. The combination of these two definitions implies the scaling for velocity $u' = u/c$, so that all velocities are in units of the speed of light. The momentum $p = \gamma mu$ has the scaling for velocity carry over, but we also add a factor of $\frac{1}{m}$, so that we have $p' = \frac{p}{mc} = \gamma\frac{u}{c}$. The electric field is scaled according to Eq. (1.8). The scaling is responsible for the lack of factors of c and m in the code.

The first lines of the code are used to define the physical characteristics of the laser pulse, such as the beam waist and pulse duration. We used the scaled electric field magnitude defined in Eq. (1.8). We use these values to make a function to define the laser field according to Eq. (2.1) and (2.2). Instead of defining the field for the entire interaction time and space, the function simply generates the field at a point in space and time when called (A.1).

The interaction time in a computational model must be finite. In order to obtain accurate results, our choice of interaction time must begin before the pulse has arrived and not end until after the electron no longer experiences the field of the laser pulse. The time interval is centered around the moment that the center of the pulse reaches the focus, at position $(0,0,0)$. We assume that the electrons are initially at rest and place 1000 randomly within the cube $\mathbf{r} = 4 \times \lambda(\pm 1, \pm 1, \pm 1)$ where w_0 is the beam waist. Note that the initial conditions are set at time $t = t_i < 0$.

These initial conditions are fed to a function for solving the trajectory of the electron (A.2). This function takes the inputs and feeds them to a built-in ODE solver. We define a right hand side function to use with the solver (A.3). The output of the ODE solver is the position and velocity arrays of the electron at the specified times.

Using the positions and times of the electron's trajectory, we are able to call the laser field

function (A.1) to define the field at each of these point. The laser is propagating in the $\theta = 0$ direction. The velocities can then be used with the laser field to define the accelerations at each time.

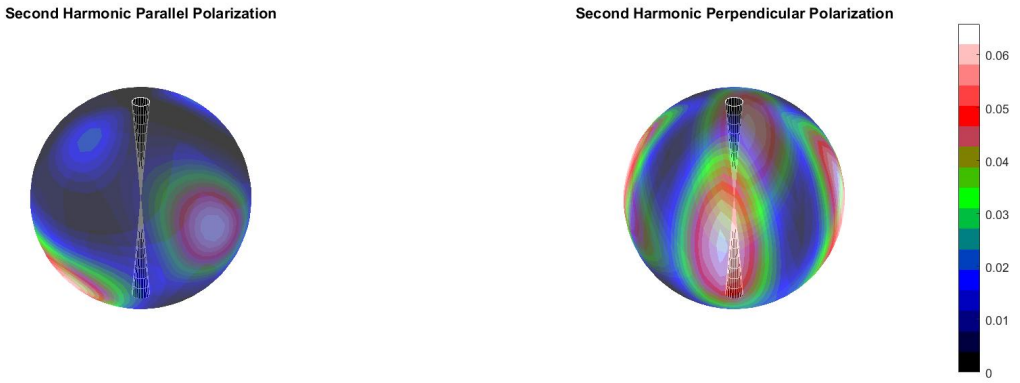

(a) **(b)**

Figure 2.1 The radiation scattered from an electron within a high intensity laser focus. The sphere is an intensity color map. The red areas are higher intensity regions and the blue areas are low intensity regions. The laser and the focus are represented by the cone in the center with the laser traveling from bottom to top. The parallel polarization is shown in (a) and the perpendicular polarization is shown in (b). The interactions of 500 randomly placed electrons with a beam corresponding to $\alpha = 0.8$ is simulated.

With the trajectories in hand we are able to calculate the scattered radiation (A.4). The scattered radiation is then Fourier transformed in order to allow us to isolate harmonics (A.5). The radiation is separated into two orthogonal polarization components, one polarization parallel to the laser propagation and one perpendicular to the beam. The polarization resolved radiation from a laser pulse is shown in Fig. 2.1. These spheres maintain many of the characteristics seen in the plane wave case discussed in Sec. 1.2.

From the spheres we can see that the polarization perpendicular to the laser beam (oriented along the equator of the sphere) is symmetric in the direction of laser propagation as well as being symmetric with respect to the polar angle. The parallel component, however, is asymmetric along

the direction of laser polarization displaying a preference for the 'downstream' side of the focus, represented by the bottom hemisphere shown in Fig. 2.1.

Our group has already done a significant amount of modeling and measurement of the radiation that is scattered around the equator of these spheres [19, 20]. These previous studies with a detector positioned at $\theta = \pi/2$ demonstrated the effectiveness of our model in describing nonlinear Thomson scattering. My investigation is focused on confirming the agreement of the model and experiment by measuring the radiation with a detector placed at $\theta = \pi/4$,'upstream' from the laser beam.

2.3 Polar Dependence Model

The angular dependence of Thomson scattering has been well documented [17, 18]. By fixing the polar angle of the detector we can model the azimuthal dependence by rotating the detectors azimuthal angle. This simulates the radiation in the the lower hemisphere in Fig. 2.1. Rotating the virtual detector gives us the patterns shown Fig. 2.2. The peak intensities in Fig. 2.2 correspond to $\alpha = 0.8$. The polarization components parallel and perpendicular to the direction of laser propagation are both shown on the plots.

As was noted in section 1.4, past research has focus on measuring the scattered radiation in the plane of the laser focus, with $\theta = \pi/2$. The model of this case is shown in Fig. 2.2(a). The perpendicular polarization displays four symmetric "leaves" as we saw in Fig. 2.1. The behavior of the parallel polarization is harder to ascertain from Fig. 2.1 and only exhibits a simple oval structure.

When a detector is placed at $\theta = \pi/4$ as in Fig. 2.2(b), the parallel polarization exhibits a significantly more complex structure. Two large lobes stretch along the $\phi = 0, \pi$ axis while two smaller lobes are beginning to emerge along the $\phi = \pi/2, 3\pi/2$ axis. The more complex structure seen by placing the detector at $\theta = 3\pi/2$ gives us benchmarks for comparing the relative positions of the two scattered polarizations. The perpendicular polarization maintains the symmetry seen in

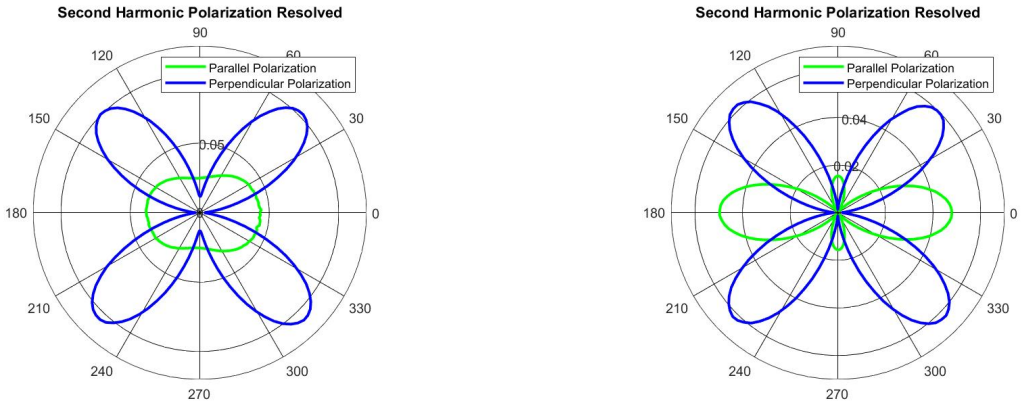

(a) **(b)**

Figure 2.2 The polarization resolved model of the second harmonic of scattered light. The interaction of 1000 electrons randomly distributed within the cube $\mathbf{r} = 4 \times \lambda[\pm 1, \pm 1, \pm 1]$ is simulated. The fields has a peak intensity corresponding to $\alpha = 0.8$. The case of a detector with $\theta = \pi/2$ is shown in (a). This case has been thoroughly researched and documented. The case of $\theta = \pi/4$ is shown in (b). The structure of the parallel polarization in (b) is significantly more complex than in (a) while the features of the perpendicular polarization remain essentially the same.

Fig. 2.2(a).

In Fig. 2.3 the case of a plane wave pulse is compared to the model's results. The peak intensities in this case correspond to $\alpha = 1.6$. Both polarizations have fourfold symmetry within the plane wave at these higher intensities. These feature are not found when the Singh model is used. When the scattered radiation at these higher intensities display the plane wave features, it can be a sign of poor focusing resulting in a larger than expected focal region.

At lower intensities, corresponding to $\alpha < 1$, the plane wave accurately predicts the polarization patterns. However, since electrons tend to be pushed out of the higher intensity regions, the plane wave calculation overestimates the intensity of the scattered radiation by a factor of 50.

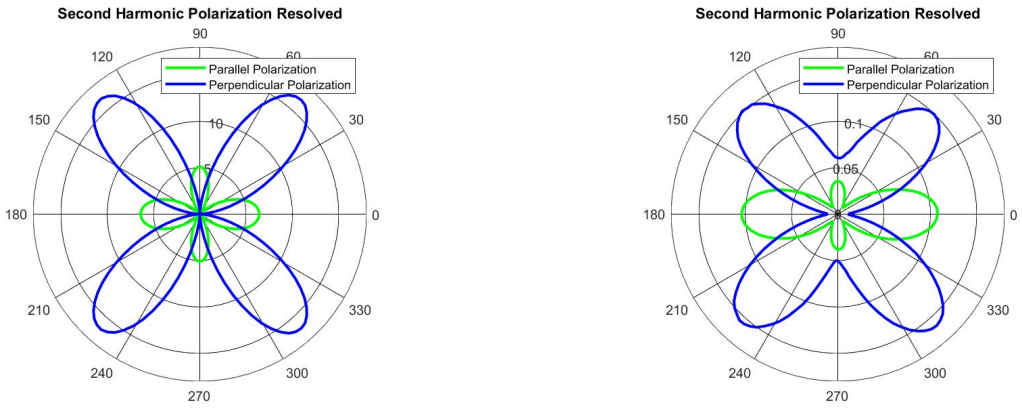

(a) **(b)**

Figure 2.3 The polarization resolved model of the second harmonic of scattered light. The interaction of 1000 electrons randomly distributed within the cube $\mathbf{r} = 4 \times \lambda[\pm 1, \pm 1, \pm 1]$ is simulated. The results of a plane wave pulse with $\alpha = 1.6$ are shown in (a). A laser beam with 160 mJ, corresponding to $\alpha = 1.6$, is used to generate (b). The parallel polarization is shown in green and the perpendicular polarization in blue. The scale shows the expected number of photons in that direction. As is evident, the plane wave produces significantly different results from the Singh model.

Chapter 3

Measurement of Polar Angle Dependence

3.1 Experiment Parameters

In order to experimentally measure nonlinear Thomson scattering, we use low pressure vacuum chambers backfilled with helium. The free electrons needed for Thomson scattering are liberated by the leading edge of the laser pulse. The pressure is kept low enough to avoid plasma effects when the gas is ionized, on the order of 10^{-2} Torr or less.

Observing nonlinear Thomson scattering requires high laser powers. And since we utilized single photon counting methods, we require a system capable of producing pulses with a repetition rates >1 Hz. The Dioclese facilities at UNL are capable of producing high repetition laser pulses with a wide range of energies capable of producing nonlinear Thomson scattering. Using their system we can observe the effects of pulses up to 160 mJ operating at 10 Hz.

The physical setup of our experimental chamber is shown in Fig. 3.1. The pulse enters the experimental chamber through a half waveplate mounted in a rotation stage. This stage is rotated to orient the linear polarization of the laser and thereby simulate the detector rotating around the focus. The laser pulse is then reflected off of a parabolic mirror and focused to an area in front of

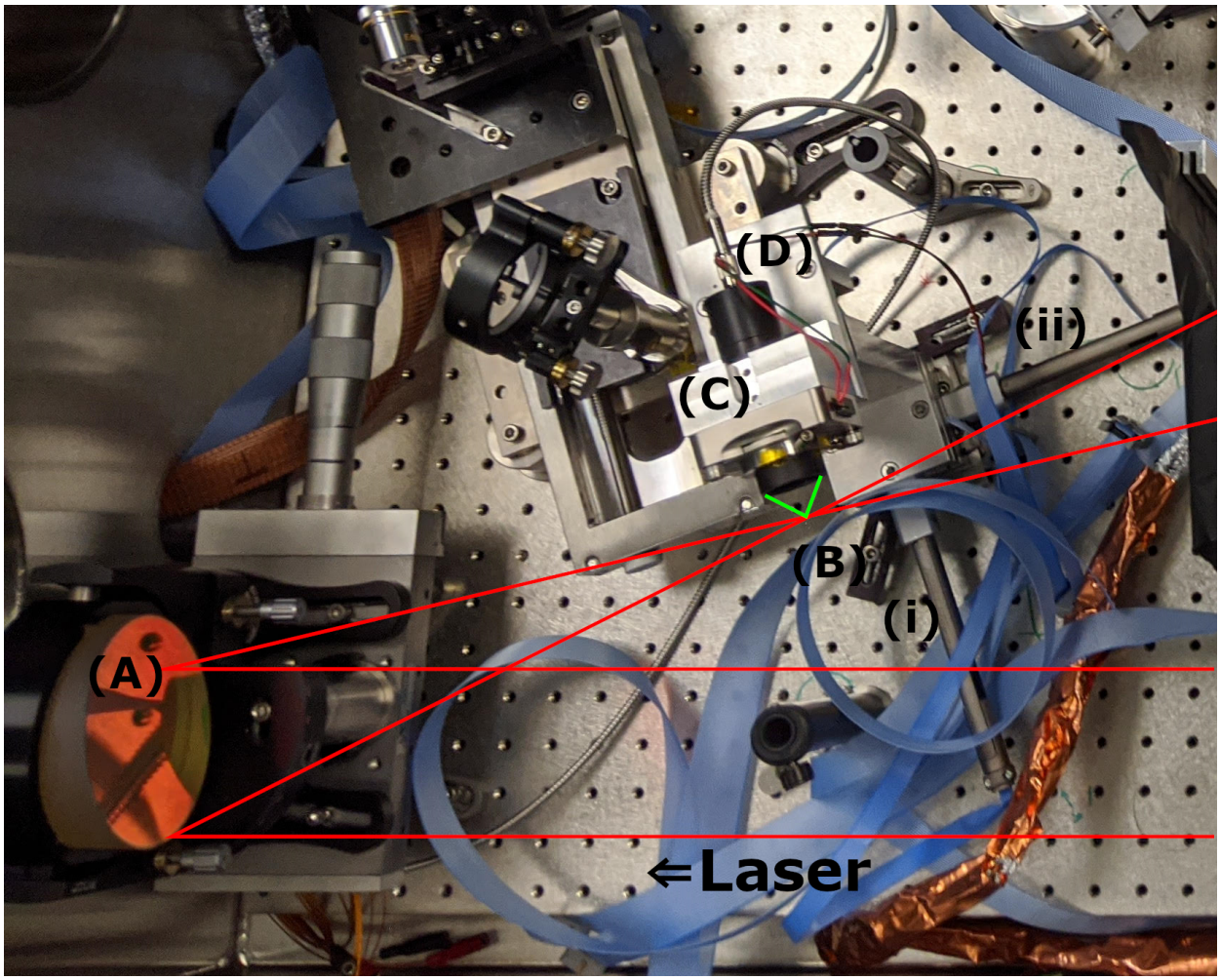

Figure 3.1 The experimental setup at UNL. The laser, represented by the red lines, enters the from the bottom left hand side of the picture and propagates to the left. It reflects off a parabolic mirror (A) and focuses at (B). The scattered light, represented by the green lines leaving the focus, passes through a polarizer and is collected in a lens tube (C) and focused onto a fiber (D). The polarizer at the front of the lens tube (C) is mounted in a rotation stage allowing us to mimic the effect of rotating the laser polarization. At the base of the collection stage you can see the actuators (i) and (ii) used to align the lens with the focus within the plane of the table. This picture shows the setup with the detector at 90 degrees.

a collection lens. The lens image the scattered light onto the end of an optical fiber. This light is then filtered to remove elements of the scattered light that are outside of the harmonic band that we observe. The transmitted photons are counted by an avalanche photo diode.

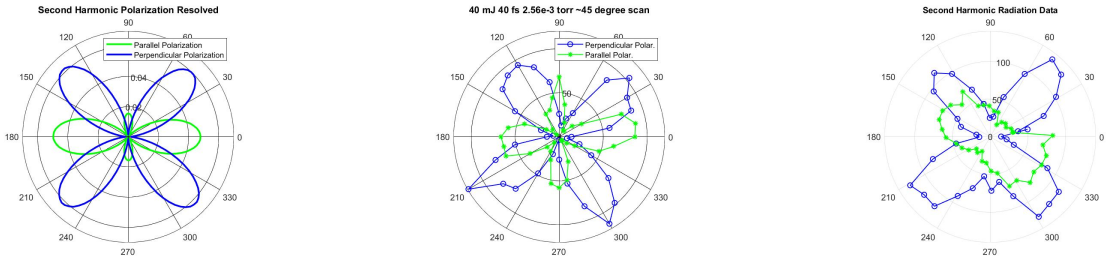

(a) **(b)** **(c)**

Figure 3.2 The model for a 40 mJ pulse with $\alpha = 0.8$ is shown in (a). The measurement for this case is shown in (b) and shows good agreement with the model. The results for the case of a detector perpendicular to the focus, at $\theta = \pi/2$, is shown in (c). The perpendicular polarization is plotted in blue with circles representing the measured data points. The parallel polarization is show in green with asterisks representing the measured data. The scale shows the number of 'hits' recorded during a 30 second scan running at 10 Hz.

We used pulses with the same physical parameters as the model, namely a 40 fs pulse with $w_0 = 3.2\ \mu$m. With a pulse energy of 40 mJ this yields a scaled field magnitude of $\alpha = 0.8$. At this intensity, we should expect the 400 nm second harmonic to be shifted to 450 nm (see Section 1.3). Our filters are centered at 450 nm $\pm$5 nm.

Single photon counting requires a large number of counts. With the laser running at 10 Hz, data is collected over a 30 second run at each setting of the waveplate. This results in a total of 300 shots for each point. The "hits" are totaled and stored in an array. The results for a 40 mJ pulse are shown next to the model in Fig. 3.2 along with the results for a detector placed at $\theta = \pi/2$. Comparing the data in Fig. 3.2b to Fig. 3.2c, we can see the smaller lobes of the parallel polarization that have emerged from the two larger lobes.

The relative angle of the polarizations of the scattered light is skewed in the data. As we examine Fig. 3.2, we see that the model predicts the "leaves" of the perpendicular polarization to be at angles of $\phi = \pi/4$ relative to the larger lobes of the parallel polarization. The lobes appear to be out of position by as much as $\pi/6$. This rotation is more pronounced for the data collected with a detector

positioned at $\theta = \pi/2$, as seen in Fig. 3.2c. The reason for this rotation is not known and is being researched by Colton Fruhling at UNL.

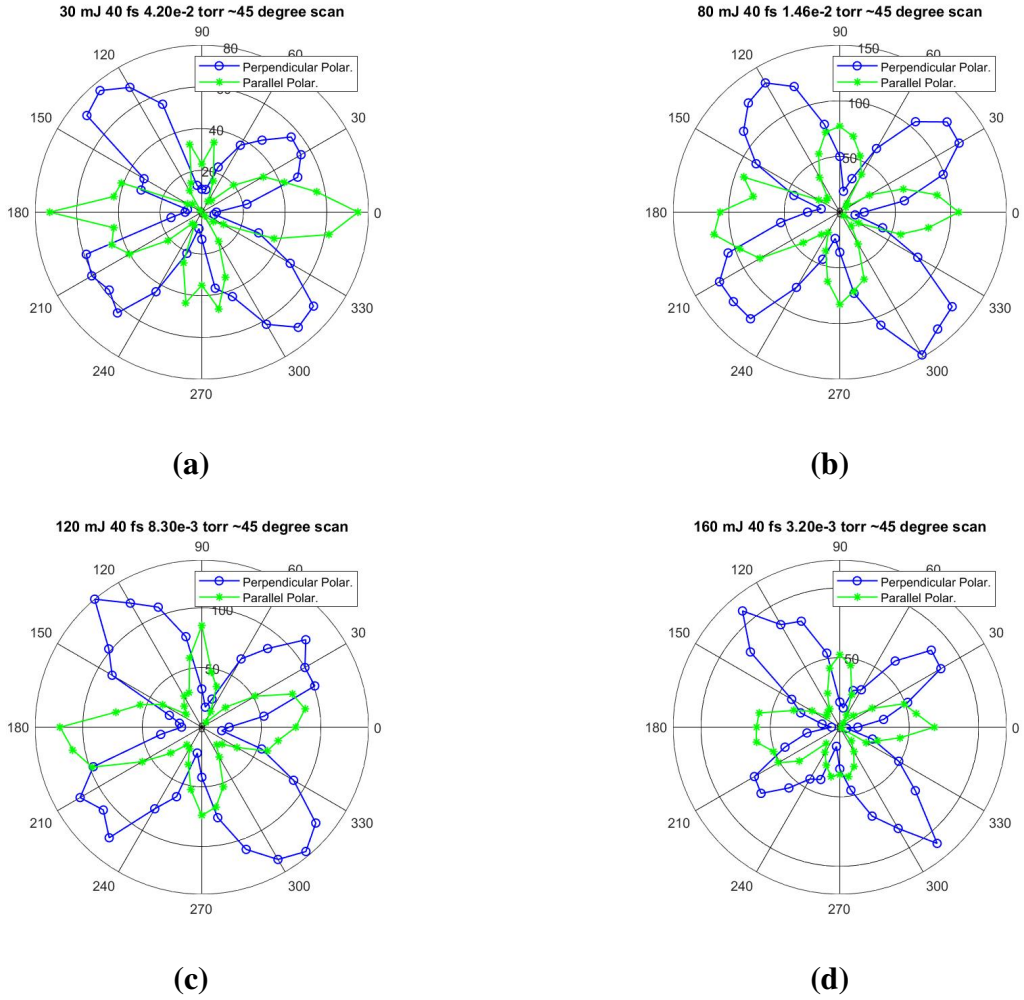

Figure 3.3 The data for the 30 mJ, 80mJ, 120 mJ, and 160 mJ measurements are shown in (a)-(d), respectively. The perpendicular polarization is plotted in blue with circles representing the measured data points. The parallel polarization is show in green with asterisks representing the measured data. The scale shows the number of 'hits' recorded during a 30 second scan running at 10 Hz.

In addition to the 40 mJ measurement, we measured the radiation scattered from 30 mJ, 80 mJ, 120 mJ, and 160 mJ pulses. The data from these measurements are shown in Fig. 3.3. These results, with the exception of the 160 mJ measurement discussed in the next section, are in good agreement

with the model. The data sets clearly display four "leaves" for the perpendicular polarization. The relative size and shape of the leaf features are accurately predicted. The parallel polarization data show two larger lobes located at $\phi = 0, \pi$ as well as smaller lobes at $\phi = \pi/2, 3\pi/2$. These are feature remain constant over the intensity range observed which matches the predictions in the model.

3.2 Conclusions

As was shown in Sec. 3.1, our model is in good agreement with the data. This agreement is seen for all of the data except the 160 mJ pulse. The model for this case is compared to the data in Fig. 3.4. We did not observe the upper and lower features of the azimuthal polarization merging as shown in the model. This discrepancy could be due to an over estimation of the intensity of the focus. This could be the result of an imperfection in the laser pulse, possibly a double pulse that splits the total energy.

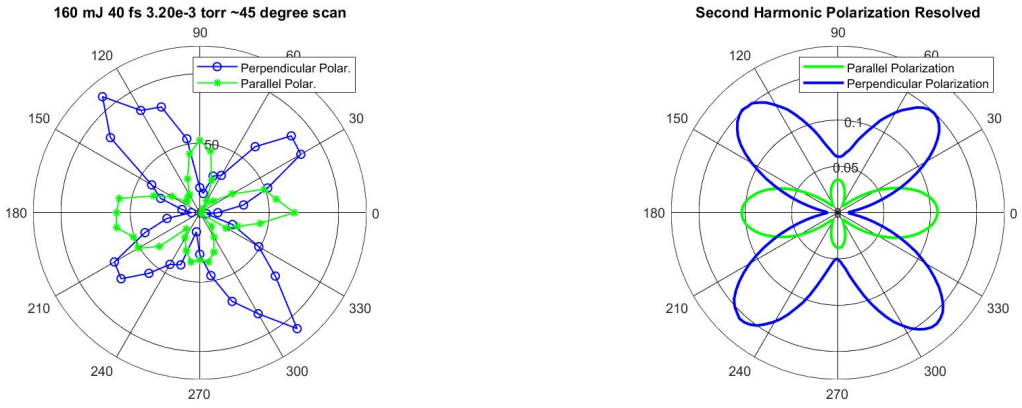

(a) **(b)**

Figure 3.4 The data for the 160 mJ measurement is show in (a). This was modeled using a beam waist of 3.2 μm produces intensities corresponding to $\alpha = 1.6$. The model is shown in (b). The model shows features in the perpendicular polarization that are not seen in the observation. This discrepancy is likely due to an over estimation of the peak intensity.

Another possible explanation is the choice of function used in estimating the size of the beam width. We used a Gaussian function to estimate the beam width to be 3.2 μm. If a sinc function is used instead, the beam waist is estimated as being 4 μm. This increase in the focal size would result in a significant decrease in intensity. The resulting scaled field magnitude for the 160 mJ pulse would be $\alpha = 1.3$. This drop in intensity results in the scattering shown in Fig. 3.5.

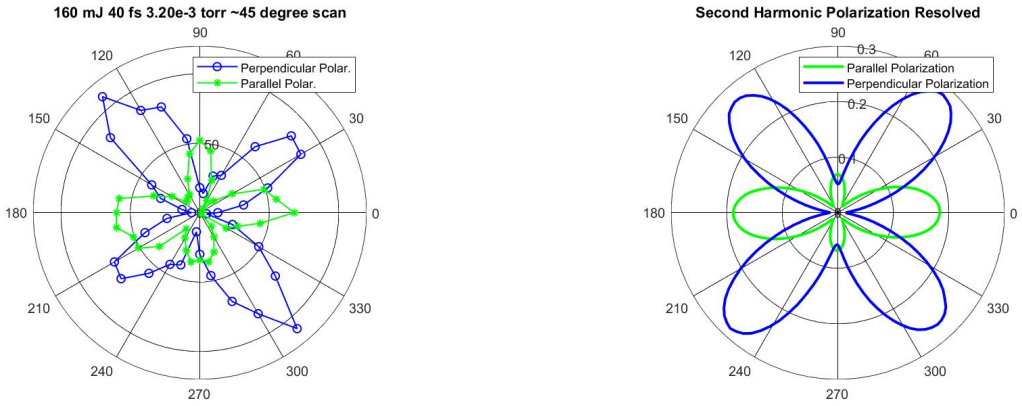

(a) **(b)**

Figure 3.5 The data for the 160 mJ measurement is show in (a). The data agrees better with the radiation pattern of the case of $w_0 = 4$ μm and $\alpha = 1.30$, shown in (b). This could be due to the focal size being overestimated or a double pulse dividing the pulse energy.

Neither of the explanations offered here would affect the model's agreement with the lower energy measurements. Further research of these higher intensity interaction will be necessary to understand the discrepancy between the model and observation.

In addition to continued research of higher intensity regimes, future measurements could include placing the detector at $\theta = \pi/4$ in order to measure the patterns shown in the lower hemisphere of Fig. 2.1. Current modeling suggests that the parallel component of the polarization should be significantly larger than the perpendicular component, as shown in Fig. 3.6. This experiment is nearly identical as outlined in Section 3.1, except the detector would be moved in the opposite direction.

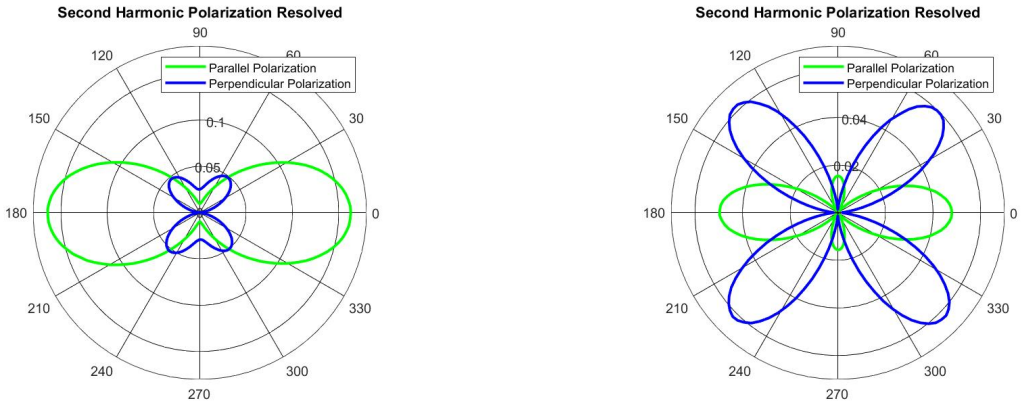

(a) **(b)**

Figure 3.6 A model of the measurement a detector at $\theta = 3\pi/4$, shown in (a). The model with $\theta = \pi/4$, investigated in this thesis, is shown in (b). These models simulated the interaction of 1000 randomly placed electrons within a laser focus with intensities corresponding to $\alpha = 0.8$.

Expansion of the model is also of interest. The current model is restricted to circular focal spots. Extending the model to accommodate more exotic focal shapes as well as astigmatic and asymmetric focal regions is of interest as well. Expanding the model would be useful as a diagnostic for high power laser focuses.

A measurement of the radiation's dependence of the polar angle would also be of interest to confirm the 'longitudinal' behavior of the radiation shown in Fig. 2.1. To the best of my knowledge, no such measurement has been reported in the literature. Performing this measurement would require the development of new detection procedures. A model of this measurement is shown in Fig. 3.7.

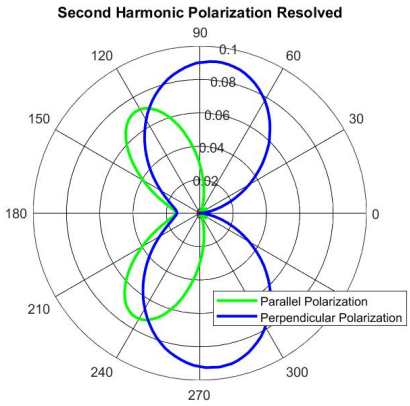

Figure 3.7 Model of scattering observed with a detector positioned at $\phi = \pi/4$ and rotating the polar angle, θ. The interaction of 1000 randomly dispersed electrons with a laser pulse with $\alpha = 0.8$. The direction of laser propagation is along the 0-180 axis. This measurement corresponds to a line of latitude in Fig. 2.1.

Appendix A

Model Code

The code for the radiation model is written in the Matlab programming language.

```
clear; % close all;
% Number of simulated electrons
num = 5;
% Interaction time
nmax = 2^9;
ti = -2*pi*25;          tf = 2*pi*25;
dt = (tf-ti)/(nmax-1);
t = ti:dt:tf;
% Size of volume in which electron's start
di = 0*2*pi*4;
% Initial positions
r0 = (2*rand(num,3) - 1)*di;
% Initial momentum
p0 = zeros(1,3);
x = zeros(num,nmax);     y = x;       z = x;
ux = x;                  uy = x;      uz = x;
ax = x;                  ay = x;      az = x;

% Calculate trajectory the electrons
for k = 1:num
% This electron's initial position
ri = r0(k,:);
% Find the trajectory of each electron
[x1,y1,z1,ux1,uy1,uz1,ax1,ay1,az1] = Trajectory(t,ri,p0);
x(k,:) = x1;             y(k,:) = y1;             z(k,:) = z1;
ux(k,:) = ux1;           uy(k,:) = uy1;           uz(k,:) = uz1;
ax(k,:) = ax1;           ay(k,:) = ay1;           az(k,:) = az1;
end

% Resolution of detector positions
jmax = 150;
p = 0:2*pi/(jmax-1):2*pi;
% Detector positions
cp = cos(p);                sp = sin(p);
st = 1/sqrt(2);             ct = 1/sqrt(2);
Nt = zeros(1,jmax);         Np = Nt;
t = repmat(t,num,1);
for j = 1:jmax
    angle = [sp(j),cp(j),st,ct];
    % Compute scattered radiation
    [Nt(j),Np(j)] = ScatteredField(t,x,y,z,ux,uy,uz,ax,ay,az,angle);
```

```
end
% Polar plot of the radiation
figure
polarplot(p,Nt,'g','LineWidth',2)
hold on
polarplot(p,Np,'b','LineWidth',2)
title('Second Harmonic Polarization Resolved')
legend({'Parallel Polarization','Perpendicular Polarization'},'Location','
    northeast')
pax=gca;    pax.GridColor = 'k';    pax.GridAlpha = 1; % Make grid black
hold off
% % % PlotSphere(t,x,y,z,ux,uy,uz,ax,ay,az)
```

A.1 Laser Field

```
function [Ex,Ey,Ez,Bx,By,Bz] = LaserField(x,y,z,t)
% Laser parameters
Ep = 0.8; % sqrt(1.5e18/(2.146e18));
w0 = 2*pi*5;
z0 = w0^2/2;
tau = 2*pi*15;

% Singh Model
Zinv = 1./(z0+1i*z);
rho2 = x.^2+y.^2;
R = z+z0^2./z;
psi = z0.*Zinv.*exp(-0.5*rho2.*Zinv);
env = exp(-(t-z-rho2./(2*R)).^2/tau^2);
plane = exp(1i*(z-t));
field = Ep*psi.*plane.*env;
Ex = real(field);
Ey = real(0.5*x.*y.*Zinv.^2.*field);
Ez = real(-1i*x.*Zinv.*field);
Bx = Ey;
By = Ex;
Bz = real(-1i*y.*Zinv.*field);

% % % Plane Wave
% % phase = z-t;
% % env = Ep*exp(-(phase).^2/tau^2);
% % Ex = env.*cos(phase);
% % Ey = 0;
% % Ez = 0;
% % Bx = 0;
% % By = Ex;
% % Bz = 0;
end
```

A.2 Electron Trajectory

```
function [x,y,z,ux,uy,uz,ax,ay,az] = Trajectory(t,r0,p0)
qi=zeros(6,1);
% Load the initial conditions for the ODE solver
qi(1:3) = r0;
qi(4:6) = p0;
ti = t(1);
tf = t(end);
% Solve the trajectory using ode45
options = odeset('RelTol',1e-4);
```

```
[temp,q] = ode45(@Lorentz,[ti,tf],qi,options);
q = MyInterp(temp,q,t,'spline'); % A stripped down version of interp1
% q = interp1(temp,q,t,'spline');
% Unload the ODE results
x = q(:,1).';        y = q(:,2).';        z = q(:,3).';
px = q(:,4).';       py = q(:,5).';       pz = q(:,6).';
gamma = sqrt(1+px.^2+py.^2+pz.^2);
ux = px./gamma;      uy = py./gamma;      uz = pz./gamma;
% Find the vector components of the laser field at current position
[Ex,Ey,Ez,Bx,By,Bz] = LaserField(x,y,z,t);
% Calculate the accelerations
uDotE = ux.*Ex+uy.*Ey+uz.*Ez;
ax = (Ex+uy.*Bz-By.*uz-ux.*uDotE)./gamma;
ay = (Ey-ux.*Bz+Bx.*uz-uy.*uDotE)./gamma;
az = (Ez+ux.*By-Bx.*uy-uz.*uDotE)./gamma;
end
```

A.3 Lorentz Force ODE RHS

```
function derivs = Lorentz(t,q)
% Unload initial conditions
x = q(1);          y = q(2);          z = q(3);
px = q(4);         py = q(5);         pz = q(6);
gamma = sqrt(1+px^2+py^2+pz^2);
ux = px/gamma;   uy = py/gamma;   uz = pz/gamma;
% Find the vector components of the laser field at current position
[Ex,Ey,Ez,Bx,By,Bz] = LaserField(x,y,z,t);
% Calculate the value of the derivatives
derivs=q*0;
derivs(1) = ux;   derivs(2) = uy;   derivs(3) = uz;
derivs(4) = Ex+uy*Bz-By*uz;
derivs(5) = Ey-ux*Bz+Bx*uz;
derivs(6) = Ez+ux*By-Bx*uy;
end
```

A.4 Scattered Radiation

```
function [Nt,Np]=ScatteredField(t,x,y,z,ux,uy,uz,ax,ay,az,angle)
sp = angle(1);  cp = angle(2);  st = angle(3);   ct = angle(4);
% Position vector in direction of detector
xd = st*cp;          yd = st*sp;          zd = ct;
% Find scattered radiation
cx = xd-ux;          cy = yd-uy;          cz = zd-uz;
gx = cy.*az-ay.*cz;  gy = -cx.*az+ax.*cz; gz = cx.*ay-ax.*cy;
D = (1-xd*ux-yd*uy-zd*uz).*(1-xd*ux-yd*uy-zd*uz).*(1-xd*ux-yd*uy-zd*uz);
% Scattered field components
Ax = (yd*gz-gy*zd)./D;  Ay = (-xd*gz+gx*zd)./D; Az = (xd*gy-gx*yd)./D;
td = t-x*xd-y*yd-z*zd;
At = ct*cp*Ax+ct*sp*Ay-st*Az;
Ap = -sp*Ax+cp*Ay;
% Find the frequency components
Nt = Spectrum(td,At);
Np = Spectrum(td,Ap);
end
```

A.5 Scattered Spectrum

```
function Nt = Spectrum(td,A)
nu1 = 1.6; % Lower frequency detected
nu2 = 2.1; % Upper frequency detected
% Fundamental: 0.8 to 1.1
% Second Harmonic: 1.6 to 2.1
% Third Harmonic: 2.1 to 3
num = size(td,1);
nmax = size(td,2);
Anu = 0*A;  nu = zeros(num,0.5*nmax+1);
for k = 1:num
    tmax = td(k,end);   tmin = td(k,1);
    dt = (tmax-tmin)/(nmax-1);
    teven = tmin:dt:tmax;
    A(k,:) = MyInterp(td(k,:),A(k,:),teven,'spline');
             % A stripped down version of interp1
%     A(k,:) = interp1(td(k,:),A(k,:),teven,'spline');
    Anu(k,:) = fft(A(k,:))*dt;
    dnu=2*pi/(dt*(nmax-1));
    nu(k,:) = 0:dnu:(0.5*nmax)*dnu;
end
Inu = abs(Anu(:,1:0.5*nmax+1)).^2/pi;
Iharm = double((nu > nu1 & nu < nu2)).*Inu;
% Integrate to find total radiation within harmonic band
ft = 0;
for k = 1:num
   ft = ft + trapz(nu(k,:),Iharm(k,:))*9.00e-4;
end
Nt = ft/(1.55*(nu2+nu1)/2);
end
```

A.6 Data Display

The code for displaying the data.

```
theta = 0:pi/18:2*pi;
countx = [29 6 7 22 49 55 56 45 37 23 11 11 13 55 69 76 72 32 31 ...
            7 8 15 59 61 58 63 44 21 8 13 37 43 62 72 70 49 29];
countz = [37 62 75 56 42 34 20 7 6 16 34 23 33 15 12 1 6 8 41 ...
            43 73 43 46 40 21 7 7 26 44 35 47 33 16 2 7 12 37];
figure
polarplot(theta, countx, 'b-o','LineWidth',1)
title('30 mJ 40 fs 4.20e-2 torr ~45 degree scan')
hold on
polarplot(theta, countz,'g-*','LineWidth',1)
legend('Perpendicular Polar.','Parallel Polar.')
pax=gca;    pax.GridColor = 'k';    pax.GridAlpha = 1; % Make grid black
hold off
```

Bibliography

[1] J.J. Thomson, “Cathode Rays." Philosophical Magazine, 44, 293 (1897).

[2] Maxwell, James Clerk, and Royal Society (Great Britain). “A Dynamical Theory of the Electromagnetic Field." The Royal Society, (1865).

[3] Lorentz, Hendrik Antoon. “Attempt of a theory of electrical and optical phenomena in moving bodies." Leiden: EJ Brill, Leiden (1895).

[4] Thomson, J. J. “Conduction of Electricity through Gases.” Cambridge Univ. Press, (1906).

[5] Kibble, T.W.B. “Mutual Refraction of Electrons and Photons,” Phys. Rev. **150**, 1060 (1966).

[6] E. S. Sarachik and G. T. Schappert. “Classical Theory of the Scattering of Intense Laser Radiation by Free Electrons,” Phys. Rev. D **1** , 2738-2753 (1970).

[7] J. H. Eberly and A. Sleepers.“Trajectory and Mass Shift of a Classical Electron in a Radiation Pulse,” Phys. Rev. **176**, 1570-1573 (1968).

[8] Donna Strickland and Gerard Mourou. “Compression of amplified chirped optical pulses,” Opt. Commun. Volume 56, Issue 3, Pages 219-221, (1985).

[9] P.H. Bucksbaum, M. Bashkansky, and T.J. McIlrath, “Scattering of Electrons by Intense Coherent Light,” Phys. Rev. Letters 58.4 (1987): 349

[10] Hartemann, F.V. et al. “Three-dimensional relativistic electron scattering in an ultrahigh-intensity laser focus,” Phys. Rev. E, 58.4 (1998): 5001.

[11] D.D. Meyerhofer, J.P. Knauer, S.J. McNaught, and C.I Moore, “Observation of relativistic mass shift effects during high-intensity laser–electron interactions,” JOSA B 13.1 (1996): 113-117.

[12] G. Malka, E. Lefebvre, and J.-L. Miquel, “Experimental observation of electrons accelerated in vacuum to relativistic energies by a high-intensity laser." Phys. Rev. Lett. 78, 3314 (1997).

[13] C.I Moore, J.P. Knauer, and D.D. Meyerhofer, “Observation of the Transition from Thomson to Compton Scattering in Multiphoton Interactions with Low-Energy Electrons,” Phys. Rev. Letters 74.13 (1995): 2439.

[14] P.H. Bucksbaum, M. Bashkansky, and T.J. McIlrath, “Scattering of Electrons by Intense Coherent Light,” Phys. Rev. Letters 58.4 (1987): 349

[15] J.X. Wang et al, “High-intensity laser-induced electron acceleration in vacuum." Phys. Rev. E 60, 7473 (1999)

[16] Yan, Wenchao, et al. “High-order multiphoton Thomson scattering." Nature Photonics 11.8 (2017): 514-520.

[17] Chen, S. Y., Maksimchuk, A., and Umstadter, D. “Experimental observation of relativistic nonlinear Thomson scattering,” Nature **396** , 653-655 (1998).

[18] Lee, Kitae, et al. "Temporal and spatial characterization of harmonics structures of relativistic nonlinear Thomson scattering." Optics Express 11.4 (2003): 309-316.

[19] Smith, D., M. Ware, and J. Peatross. "Linear and Nonlinear Thomson Scattering Observed Perpendicular to a Relativistic Laser Focus." Frontiers in Optics. Optical Society of America, 2015.

[20] Ware, M., et al. "Polarization-Resolved Single-Photon Measurements of Nonlinear Thomson Scattering." Laser Science. Optical Society of America, 2019.

[21] Michael Ware et al., " Measured photoemission from electron wave packets in a strong laser field," Opt. Lett. 41 (4), 689-692 (2016).

[22] Lau, Y.Y. "Nonlinear Thomson scattering: A tutorial." Physics of Plasmas **10**, 2155 (2003)

[23] David. J. Griffiths. *Introduction of Electrodynamics*, 3rd ed., Prentice Hall (1999).

[24] Brice Quesnel and Patrick Mora, "Theory and simulation of the interaction of ultraintense laser pulses with electrons in vacuum." Phys. Rev. E 58.3 (1998): 3719.

[25] V. S. Ignatovsky, "The relationship between geometric and wave optics and diffraction of an azimuthally symmetric beam," Trans. Opt. Inst. Petrograd **1**, paper 3 (1920).

[26] V. S. Ignatovsky, "Diffraction by a lens with arbitrary aperture," Trans. Opt. Inst. Petrograd **1**, paper 4 (1920).

[27] V. S. Ignatovsky, "Diffraction by a parabolic mirror having arbitrary opening," Trans. Opt. Inst. Petrograd **1**, paper 5 (1920).

[28] Peatross, Justin, et al. "Vector fields in a tight laser focus: comparison of models." Optics express 25.13 (2017): 13990-14007.

[29] W. Erikson and S. Singh. "Polarization properties of Maxwell-Gaussian laser beams," Phys. Rev. E **49**, 5778–5786 (1994).